nature physics

ARTICLES

https://doi.org/10.1038/s41567-017-0035-2

Robust integer and fractional helical modes in the quantum Hall effect

Yuval Ronen, Yonatan Cohen, Daniel Banitt, Moty Heiblum* and Vladimir Umansky

Electronic systems harboring one-dimensional helical modes, where spin and momentum are locked, have lately become an important field of their own. When coupled to a conventional superconductor, such systems are expected to manifest topological superconductivity; a unique phase hosting exotic Majorana zero modes. Even more interesting are fractional helical modes, yet to be observed, which open the route for realizing generalized parafermions. Possessing non-Abelian exchange statistics, these quasiparticles may serve as building blocks in topological quantum computing. Here, we present a new approach to form protected one-dimensional helical edge modes in the quantum Hall regime. The novel platform is based on a carefully designed double-quantum-well structure in a GaAs-based system hosting two electronic sub-bands; each tuned to the quantum Hall effect regime. By electrostatic gating of different areas of the structure, counter-propagating integer, as well as fractional, edge modes with opposite spins are formed. We demonstrate that, due to spin protection, these helical modes remain ballistic over large distances. In addition to the formation of helical modes, this platform can serve as a rich playground for artificial induction of compounded fractional edge modes, and for construction of edge-mode-based interferometers.

Pursuing Majorana zero modes (MZMs) in condensed matter physics is gaining wide range interest[1–9]. While bearing some resemblance to their high-energy counterparts, condensed matter MZMs are significantly different as they are expected to possess non-Abelian exchange statistics, which renders them potential candidates for topologically protected qubits[2,10–15]. One of the most promising platforms for the formation of MZMs is a one-dimensional helical system coupled to an s-wave superconductor[16,17]. In a helical system, electrons moving in opposite directions possess opposite spins (spin degeneracy is lifted), while the two original spin species are still present. Their coupling to an s-wave superconductor induces topological, 'spinless', p-wave pairing. At the two ends of the induced superconductor, two localized MZMs are expected to form. Even more interesting are the generalized parafermions, which are expected to emerge when coupling a conventional superconductor to helical modes in the fractional quantum Hall effect (QHE) regime[18–20].

Most of the present attempts to form helical modes concentrate in materials with strong spin–orbit coupling[5–9,21–25]. While signatures of localized MZMs appear, the helical nature of the underlying modes is not confirmed. Recently, the presence of helical edge modes was reported in small (of edge length ~350 nm) two-dimensional topological insulators[21–23], as well as in a twisted bilayer graphene in the integer QHE regime (of size ~15 μm)[26]. Another work attempted to form helical modes by doping with magnetic impurity quantum wells and electrostatically inducing ferromagnetic transitions[27]. However, in these works spin protection from backscattering was not reported and strong intermode mixing limited the propagation length. Moreover, the formation of fractional helical modes has not been reported yet.

We developed a new platform that enables formation of robust and highly controllable helical modes in the QHE effect regime. The platform is based on a two-dimensional electron gas (2DEG) embedded in a double quantum well (DQW), which hosts two electronic sub-bands. By a proper electrostatic gating of two adjacent half-planes of the 2DEG, spin-split Landau levels (LLs), belonging to the different sub-bands, cross each other at the interface between the two half-planes, forming counter-propagating edge modes in the same lateral position. When the intersecting LLs are of opposite spins, the formed counter-propagating modes are helical.

One should note the difficulty in obtaining counter-propagating edge states with opposite spins in the QHE regime (see Supplementary Information - 1; SI1). Several works dating back to 1988 have demonstrated same-spin counter-propagating edge profile by utilizing a series of alternating filling factors[28]. In such

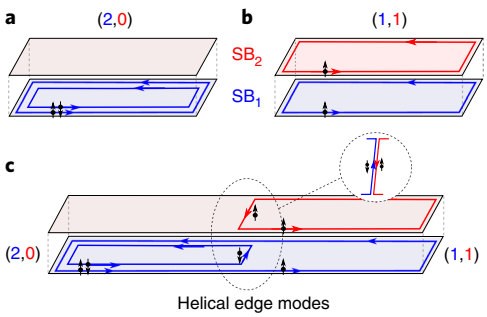

Fig. 1 | Schematic illustration of the concept of creating helical edge modes in a double-layer QHE system. Two 2DEGs are shown, one in blue denoted by SB_1, and one in red denoted by SB_2. Each 2DEG has its own filling factor, ν_1 and ν_2, respectively. The generalized filling is denoted $\nu=(\nu_1, \nu_2)$. **a**, Scenario of $\nu=(2, 0)$, with two edge modes propagating at the edge of SB_1. **b**, Scenario of $\nu=(1, 1)$, with one edge mode propagating at the edge of SB_1 and one at the edge of SB_2. **c**, The left half-plane is in $\nu=(2, 0)$ and the right half-plane is in $\nu=(1, 1)$. This creates counter-propagating edge modes with opposite spins at the interface between the two half-planes (see inset).

Braun Center for Submicron Research, Department of Condensed Matter Physics, Weizmann Institute of Science, Rehovot, Israel. Yuval Ronen and Yonatan Cohen contributed equally to this work. *e-mail: moty.heiblum@weizmann.ac.il

© 2018 Macmillan Publishers Limited, part of Springer Nature. All rights reserved.

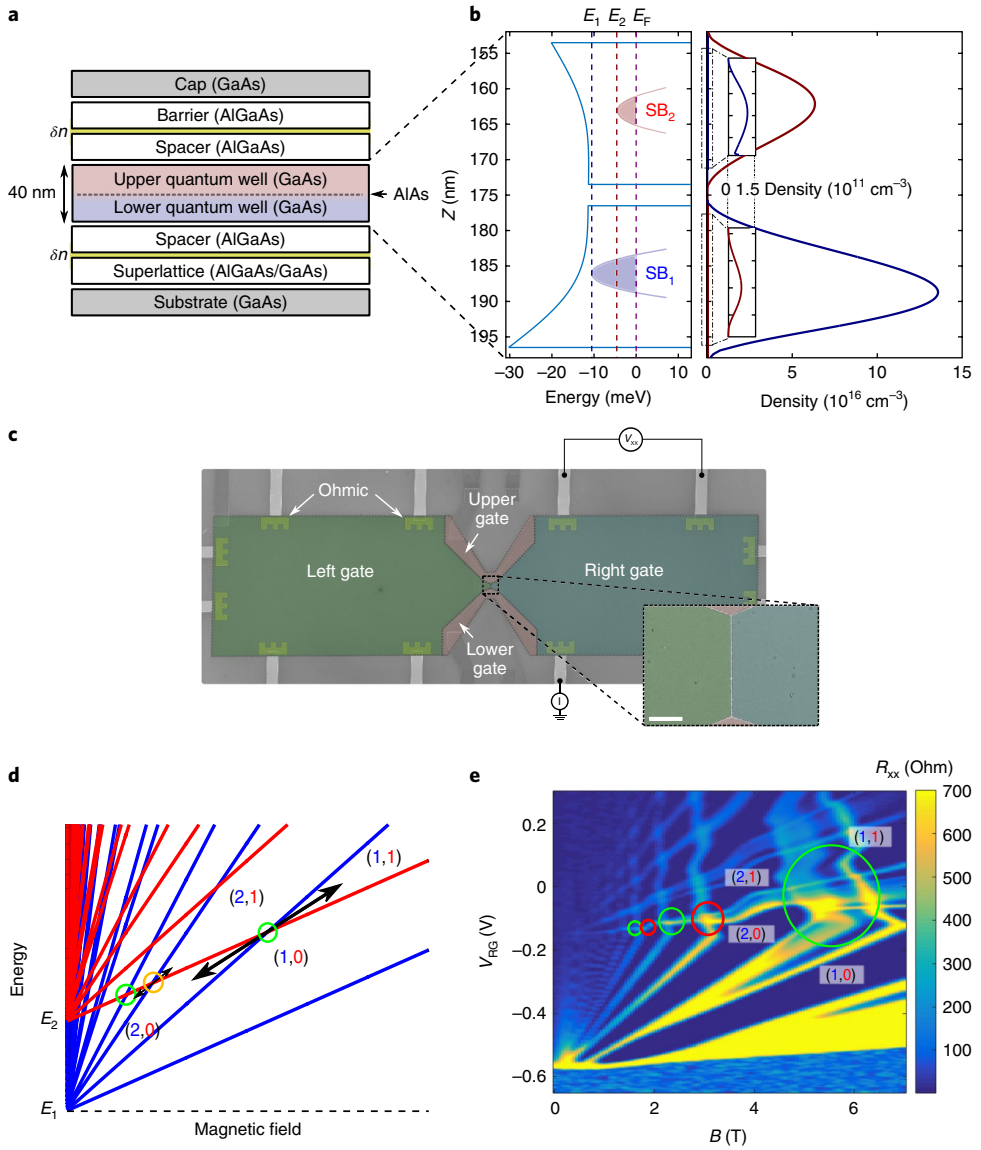

Fig. 2 | MBE growth sequence, lithographic patterning and actual fan diagram. a, Growth sequence of the DQW heterostructure. The lower and upper GaAs quantum wells are coloured in blue and red, respectively. Each well is about 20 nm wide with a 3 nm AlAs barrier separating them. **b**, NextNano3 simulation of the potential landscape and the SBs' energies as well as charge distributions at zero magnetic field. The simulation was done with a total density of 2.2×10^{11} cm^{-2}, which is in the range of densities and magnetic field relevant to filling factors $\nu=1$–4. Densities in the two sub-bands are about 1.5 and 0.7×10^{11} cm^{-2} in SB_1 and SB_2, respectively. **c**, False-colour SEM image of the device. The mesa is 800 μm long and 200 μm wide with a narrower region of 7 μm in the center, where the left and right top gates interface. The inset shows a zoom on the interface between the left and right top gates where the helical edge modes are designed to emerge (scale bar 2 μm). Note that the four top gates allow the configurations to be changed with the gates' voltage and thus also increase the propagation length of the counter-propagating modes. **d**, Ideal energy fan diagram for the two-layer 2DEG. The energies of the LLs of SB_1 (blue) and SB_2 (red) are plotted as a function of magnetic field. **e**, Measurement of the longitudinal resistance, R_{xx}, of the right half of the device as a function of magnetic field and gate voltage V_{RG}. The circles mark regions of LLs crossings with either opposite spins (green circles) or same spins (red circles). Measurements were made at a base temperature of 15 mK.

realizations helical state scenarios are not accessible. In this work we demonstrate complete control over individual edge mode spins, in both the integer and the fractional regime.

Figure 1 illustrates schematically the formation of helical edge modes in the two sub-bands of the quantum Hall system. The sub-bands, denoted by SB_1 and SB_2, are depicted as two two-dimentional sheets (blue for SB_1 and red for SB_2). Each sub-band splits into discrete LLs at high magnetic field, with individual filling factors, ν_1 in SB_1 and ν_2 in SB_2, and a generalized defined filling factor $\nu=(\nu_1, \nu_2)$. Figure 1a,b describes the scenarios of $\nu=(2, 0)$ and $\nu=(1, 1)$, respectively. When these two configurations are placed one next to the other, as shown in Fig. 1c, counter-propagating chiral edge modes, with opposite spins, propagate along the interface (spin down in SB_1, blue, and spin up in SB_2, red), manifesting integer helical edge modes.

Figure 2a shows a schematic illustration of the heterostructure used to implement the two-sub-band system. A 40 nm thick GaAs layer, clad on the top and bottom by AlGaAs layers, forms the quantum well structure. A thin AlAs barrier, 3 nm thick, is inserted in the middle of the GaAs layer to form a DQW potential landscape. The total areal density at zero gate voltage is $n=2.7\times10^{11}$ cm^{-2} and the low-temperature mobility is $\mu=0.6\times10^{6}$ cm^2 V^{-1} s^{-1}. Modulation

© 2018 Macmillan Publishers Limited, part of Springer Nature. All rights reserved.

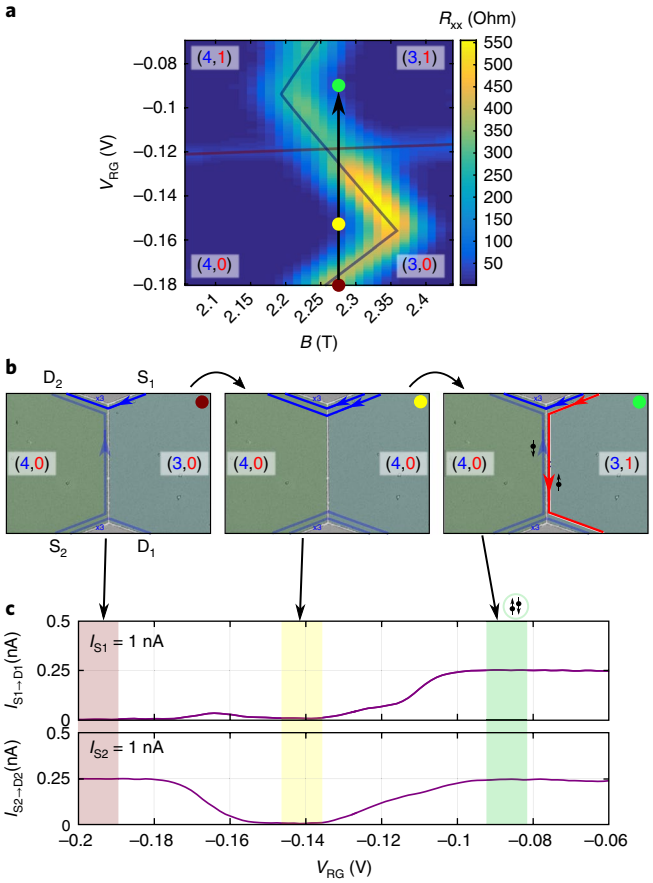

Fig. 3 | Tuning the structure to host integer helical modes. a, Longitudinal resistance, R_{XX}, of the right half-plane of the device as a function of magnetic field and gate voltage, V_{RG}, near the (4, 0) → (3, 1) transition. **b**, An illustration of the edge modes when the left-hand side is set to (4, 0) and the right-hand side is scanned along the black arrow, i.e. from (3, 0) (red point) through (4, 0) (yellow point) to (3, 1) (green point). **c**, The top graph corresponds to the measured reflected current in D_1 when a current of 1 nA is injected at contact S_1, with the left half-plane held at (4, 0) and the gate voltage V_{RG} scanned. The red, yellow and green shaded regions mark the range of gate voltage leading to fillings (3, 0), (4, 0) and (3, 1) in the right half-plane. The bottom figure shows the measured current at D_2 when 1 nA is injected at S_2. Coloured regions were chosen according to $R_{XX} = 0$.

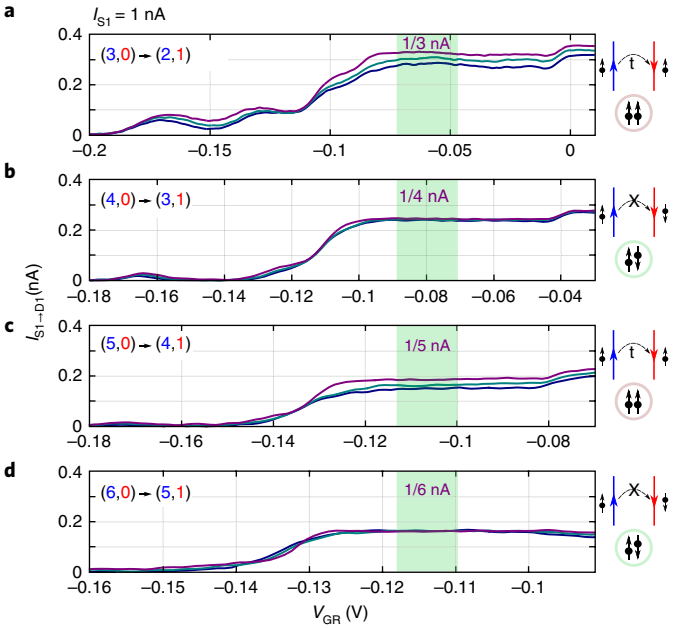

Fig. 4 | Spin-protected intermode tunnelling. a–d, Measurements of the reflected current reaching contact D_1 when current is injected at contact S_1 for different filling factors. In all measurements the left half-plane is held at (n, 0) while the right half-plane is scanned from (n − 1, 0), through (n, 0) to (n − 1, 1), where n = 3, 4, 5 and 6 in **a**, **b**, **c** and **d**, respectively. The green shaded regions mark the gate voltage range in which counter-propagating intersecting edge modes are formed. The different colours, purple, green and blue, correspond to three propagation lengths, L_{CP} = 7, 150 and 300 μm, respectively. When n is odd the two edge modes have the same spin, while where n is even the two edge modes have opposite spins. While inter-mode tunnelling is evident for same-spin configurations, transport remains ballistic even for L_{CP} = 300 μm for opposite-spin configurations.

doping, predominantly at the lower side of the DQW, leads to a tilted potential in the well (self-consistent simulation in Fig. 2b). A top-view scanning electron microscopy (SEM) image in Fig. 2c shows a fabricated structure with its top gates, dividing the surface into two adjacent half-planes. All measurements were made at a base temperature of 15 mK using a standard lock-in technique at a frequency of 37 Hz. Each line, located on the cold finger of the cryostat and cooled to base temperature, was filtered by a cascade of three pi-filters followed by an *RC* filter.

The fundamental difficulty in realizing the proposed configuration is illustrated schematically in Fig. 2d, where a naive illustration of the energy dependence of the LLs (in SB_1 and in SB_2) is plotted as function of magnetic field. Two different generalized fillings, e.g. (2, 0) and (1, 1), each in a different half-plane, cannot coexist in a single magnetic field. However, in practice the situation is different. As the energies of different LLs (in different sub-bands) cross, charge must redistribute between the sub-bands[29,30]. The charge redistribution leads to bending of the linear-like evolution of the LLs' fan diagram, allowing, under a proper design, for two generalized fillings (with equal sums of the individual fillings on both sides) to take place at the same magnetic field (Fig. 2e). Note that charge transfer costs an additional energy since it leads to built-in electric field that charges the mutual capacitance between the two regions of the DQW where the different LLs reside—thus partly opposing the charge transfer[29,30]. A narrower DQW is desirable for a larger charge transfer, and thus a more pronounced bending of the LLs with magnetic field away from the linear evolution.

The fan diagram of the longitudinal resistance (which follows the actual evolution of the LLs) is plotted in Fig. 2e. As the top gate voltage rises above −0.15 V, LLs gradually fill, and charge transfers from SB_1 to SB_2 (as LLs cross). LLs in SB_1 lose carriers, thus shifting to lower magnetic fields (having a negative slope around the crossing regions). In the present configuration, there are multiple filling fractions between $\nu = 2$ and $\nu = 1$; hence, the charge transfer near the crossings of LLs is not large enough to allow a gate-controlled transition (2, 0) → (1, 1), yet a transition (4, 0) → (3, 1) can be achieved (Fig. 3a). With $B = 2.075$ T and $V_{LG} = -0.158$ V, the filling factor in the left half-plane is $\nu = (4, 0)$, while scanning V_{RG} along the black arrow varies the filling on the right, (3, 0) → (4, 0) → (3, 1) (Fig. 3b).

A current of 1 nA is injected at S_1 and its reflected part, $I_{S1\to D1}$, is plotted in Fig. 3c (upper panel). With the left half-plane at (4, 0), and the right half-plane tuned to (3, 0) or (4, 0), all the injected edge modes circulate the outer perimeter of the two-dimensional plane, arriving at D_2, while $I_{S1\to D1} = 0$. When the right half-plane is tuned to (3, 1), three edge modes arrive at D_2 while a helical mode flows

© 2018 Macmillan Publishers Limited, part of Springer Nature. All rights reserved.

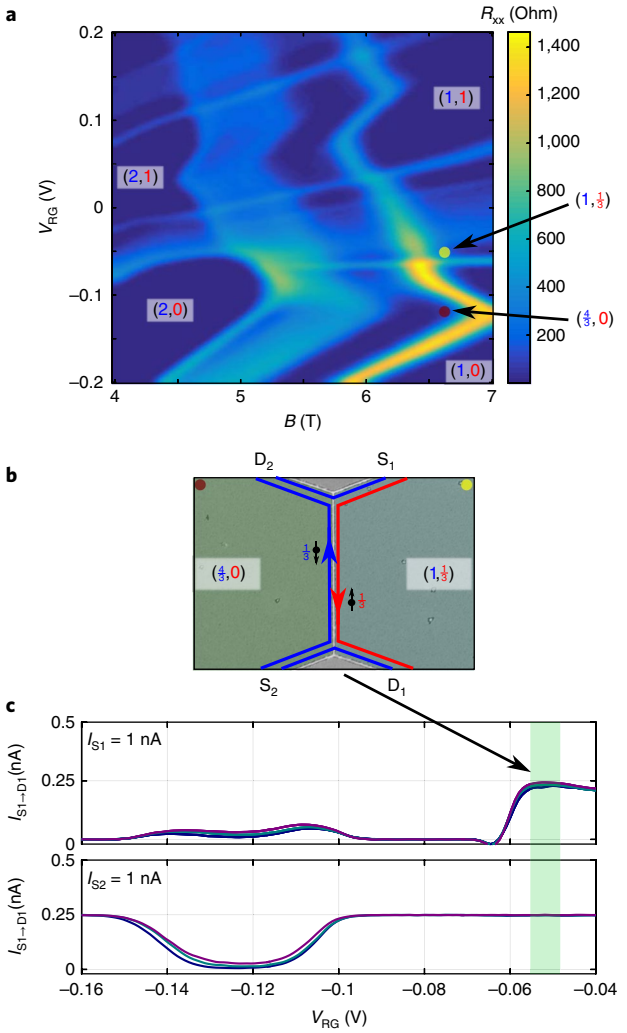

Fig. 5 | Formation of fractional helical states. a, Fan diagram of the longitudinal resistance, R_{XX}, of the right half-plane of the device as a function of magnetic field and gate voltage, V_{RG}, in the transition region (2, 0) → (1, 1). Fractional quantum Hall states are clearly observed within the regions of the integer states. The red and yellow dots correspond to filling factors (4/3, 0) and (1, 1/3), respectively. **b**, An illustration of the formed fractional helical modes. **c**, The top (bottom) graph displays the current reaching D_1 (D_2) when current is injected at S_1 (S_2), while the left half-plane is tuned to (4/3, 0) and the right half-plane is scanned. The green shaded regions correspond to the voltage range in which the right-hand side is at (1, 1/3). Both currents reach 0.25 nA (with the 1/3 mode being fully reflected at both half-planes). The colours purple, green and blue correspond to three propagation lengths, L_{CP} = 7, 150 and 300 μm, respectively.

across the interface. One edge mode (LL in SB_2, red line in right-hand figure of Fig. 3b) is fully reflected to D_1, with $I_{S1\to D1}$ = 0.25 nA. Similarly, injecting current at S_2 and measuring $I_{S2\to D2}$ leads to a complementary result (Fig. 3c, lower panel). These observations agree with ballistic propagation of helical modes without intermode scattering (Fig. 3c, green shaded region).

The transition (4, 0) → (3, 1) is evidently only one example where interlayer charge transfer is sufficiently large to allow the formation of helical modes. Figure 2e shows four such transitions(n, 0) → (n − 1, 1) with n = 3, 4, 5, 6, which allow gate-controlled transitions (open circles). Transitions with an even n, such as (4, 0) → (3, 1) and (6, 0) → (5, 1) (green circles), lead to helical modes. Same-spin counter-propagating modes are born with the transitions (3, 0) → (2, 1) or (5, 0) → (4, 1) (red circles).

In Fig. 4 measurement results of $I_{S1\to D1}$ are plotted for the four transitions in devices with three different counter-propagation lengths, L_{CP} = 7 μm, 150 μm and 300 μm. A clear difference is observed between same-spin transitions (odd, 0) → (even, 1) and opposite-spin transitions (even, 0) → (odd, 1). In the former case, as L_{CP} increases beyond 7 μm a reduction in $I_{S1\to D1}$ is observed. The reduction in $I_{S1\to D1}$ is fully compensated by an increase in $I_{S1\to D2}$ (see Supplementary Information, section S1), proving that intermode equilibration takes place (due to tunnelling), with equilibration length of about 1 mm (with no bulk current). In contrast, when helical modes are formed, no reduction in $I_{S1\to D1}$ is observed, even for L_{CP} = 300 μm—demonstrating spin protection. (Additional measurements can be found in SI2.)

We turn to the fractional regime and concentrate on R_{XX} in the B–V_{RG} plane around the (2, 0) → (1, 1) transition (Fig. 5a). The red and yellow dots, which stand for (4/3, 0) and (1, 1/3), respectively, allow an intersection of counter-propagating edge modes with opposite spins, each with filling ν = 1/3 (Fig. 5b). Indeed in the appropriate range of V_{RG}, the currents $I_{S1\to D1}$ and $I_{S2\to D2}$ are both found to be 0.25 nA (Fig. 5c, green regions). Note that while $I_{S2\to D2}$ is not affected by the propagation length, $I_{S1\to D1}$decreases slightly as the propagation length increases. Since a corresponding increase in $I_{S1\to D2}$ is not observed, the missing current evidently flows through the bulk of the right half-plane due to a finite R_{XX} (see SI3).

Finally, by directly contacting the helical modes, establishing thus a common Fermi energy in the two counter-propagating modes (Fig. 6a), four-terminal measurements can be made (Fig. 6b). Current I is injected in contact 3 while contacts 1, 2 and 6 are grounded. The ratio between the potential difference between contacts 4 and 5, V_{45}, and the current I is the appropriate trans-resistance. The resistance V_{45}/I is plotted as a function of the magnetic field in Fig. 6d, for V_{LG} = −0.158 V and V_{RG} = −0.09 V (denoted by the white dashed lines in Fig. 6c). At low and high magnetic fields, with the transitions (4, 0) → (4, 1) and (3, 0) → (3, 1), only a single chiral channel carries the current along the interface between the two regions; hence, V_{45} = 0. However, in the helical regime, for the transition (4, 0) → (3, 1), two counter-propagating edge modes carry the currents between the contacts and $V_{45}/I = \frac{R_Q}{4}$, where $R_Q = \frac{h}{e^2}$, in a good agreement with the expected trans-resistance.

The embedded 2DEG in GaAs–AlGaAs heterostructures has not played a significant role thus far in the emergent field of topological insulators and topological superconductors (aside, of course, from the illustrious QHE). This is a direct result of the very weak spin–orbit coupling in GaAs and the difficulties in inducing superconductivity in the buried 2DEG. Yet, the advantage of high-mobility electrons, the ease of processing complex structures and the well-established robust QHE states (integer and fractional) make this material system highly attractive. Here, by employing a DQW in the integer and fractional QHE regime, robust and strongly protected ballistic helical-like modes are formed. Moreover, the spin protection provided by the helical modes is shown to increase the ballistic propagation length (without intermixing) significantly.

In addition to inducing superconductivity in the two-dimensional electrons, and thus forming Majorana quasiparticles or parafermions, this versatile implementation also lends itself to hosting non-Abelian quasiparticles in topological defects, which do not require induced superconductivity[31]. Moreover, this platform can serve as a versatile playground for investigating compounded QH edge modes and arbitrarily tune the intermode interaction. For example, the spontaneous emergent of counter-propagating QH edge modes, such as hole-conjugate states (e.g. ν = 2/3, polarized and unpolarized, see SI4), can be artificially created by intersecting

© 2018 Macmillan Publishers Limited, part of Springer Nature. All rights reserved.

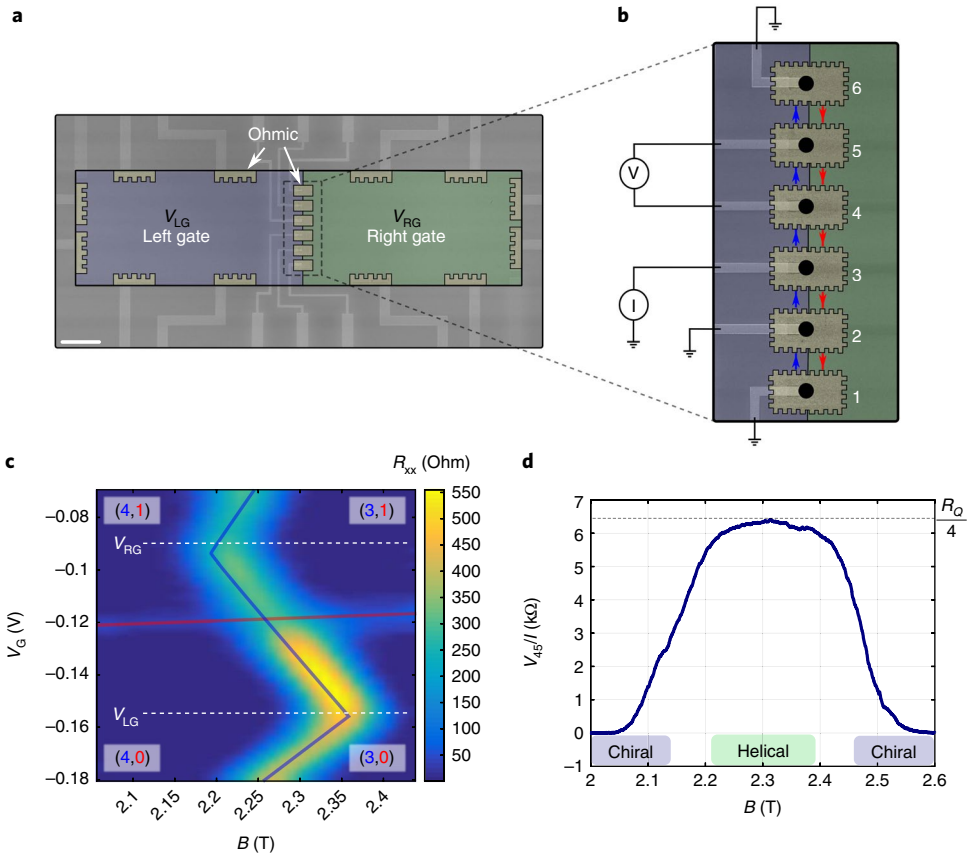

Fig. 6 | Contacting the helical edge modes directly. a, False-colour SEM image of the device. Six alloyed ohmic contacts at the interface between the left-hand gate (purple) and the right-hand gate (green). **b**, A zoom-in SEM image on the region of the contacts with the measurement scheme. Current is injected at contact 3 and voltage is measured between contacts 4 and 5, V_{45}, while the other contacts are grounded. **c**, The longitudinal resistance, R_{XX}, of the right half-plane is plotted as a function of magnetic field and gate voltage, V_{RG}, on the right-hand side near the transition (4, 0) → (3, 1). **d**, Evolution of the voltage V_{45} as a function of the magnetic field, with V_{RG} and V_{LG} fixed (white dashed lines in **c**). In the range of magnetic field where only a single chiral edge mode propagates along the interface, $V_{45}=0$. In the field range where helical edge modes form, $V_{45}/I=R_Q/4$—as expected.

$\nu=1$ and $\nu=-1/3$ states in a highly controlled fashion, thus allowing testing of the transition from the—never observed—upstream current mode to an upstream neutral mode[32–34].

Methods

Methods, including statements of data availability and any associated accession codes and references, are available at https://doi.org/10.1038/s41567-017-0035-2.

Received: 10 August 2017; Accepted: 10 December 2017;
Published online: 22 January 2018

References

1. Kitaev, A. Y. Unpaired Majorana fermions in quantum wires. *Phys. Usp.* **44**, 131–136 (2001).
2. Kitaev, A. Y. Fault-tolerant quantum computation by anyons. *Ann. Phys.* **303**, 2–30 (2003).
3. Fu, L. & Kane, C. L. Superconducting proximity effect and Majorana fermions at the surface of a topological insulator. *Phys. Rev. Lett.* **100**, 96407 (2008).
4. Alicea, J. New directions in the pursuit of Majorana fermions in solid state systems. *Rep. Prog. Phys.* **75**, 76501 (2012).
5. Mourik, V. et al. Signatures of Majorana fermions in hybrid superconductor–semiconductor nanowire devices. *Science* **336**, 1003–1007 (2012).
6. Rokhinson, L. P., Liu, X. & Furdyna, J. K. The fractional a.c. Josephson effect in a semiconductor–superconductor nanowire as a signature of Majorana particles. *Nat. Phys.* **8**, 795–799 (2012).
7. Deng, M. T. et al. Anomalous zero-bias conductance peak in a Nb–InSb nanowire–Nb hybrid device. *Nano Lett.* **12**, 6414–6419 (2012).
8. Churchill, H. O. H. et al. Superconductor-nanowire devices from tunneling to the multichannel regime: zero-bias oscillations and magnetoconductance crossover. *Phys. Rev. B* **87**, 241401 (2013).
9. Das, A. et al. Zero-bias peaks and splitting in an Al–InAs nanowire topological superconductor as a signature of Majorana fermions. *Nat. Phys.* **8**, 887–895 (2012).
10. Kitaev, A. Anyons in an exactly solved model and beyond. *Ann. Phys.* **321**, 2–111 (2006).
11. Karzig, T. et al. Scalable designs for quasiparticle-poisoning-protected topological quantum computation with Majorana zero modes. *Phys. Rev. B* **95**, 235305 (2017).
12. Das Sarma, S., Freedman, M. & Nayak, C. Majorana zero modes and topological quantum computation. *NPJ Quant. Inf.* **1**, 15001 (2015).
13. Clarke, D. J., Sau, J. D. & Das Sarma, S. A practical phase gate for producing bell violations in Majorana wires. *Phys. Rev. X* **6**, 21005 (2016).
14. Nayak, C., Simon, S. H., Stern, A., Freedman, M. & Das Sarma, S. Non-Abelian anyons and topological quantum computation. *Rev. Mod. Phys.* **80**, 1083–1159 (2008).
15. Cheng, Q. B., He, J. & Kou, S. P. Verifying non-Abelian statistics by numerical braiding Majorana fermions. *Phys. Lett. A* **380**, 779–782 (2016).
16. Lutchyn, R. M., Sau, J. D. & Das Sarma, S. Majorana fermions and a topological phase transition in semiconductor–superconductor heterostructures. *Phys. Rev. Lett.* **105**, 77001 (2010).
17. Oreg, Y., Refael, G. & Von Oppen, F. Helical liquids and Majorana bound states in quantum wires. *Phys. Rev. Lett.* **105**, 177002 (2010).
18. Vaezi, A. Superconducting analogue of the parafermion fractional quantum Hall states. *Phys. Rev. X* **4**, 31009 (2014).
19. Clarke, D. J., Alicea, J. & Shtengel, K. Exotic non-Abelian anyons from conventional fractional quantum Hall states. *Nat. Commun.* **4**, 1348 (2013).
20. Lindner, N. H., Berg, E., Refael, G. & Stern, A. Fractionalizing Majorana fermions: non-abelian statistics on the edges of abelian quantum Hall states. *Phys. Rev. X* **2**, 41002 (2012).

© 2018 Macmillan Publishers Limited, part of Springer Nature. All rights reserved.

21. König, M. et al. Quantum spin Hall insulator state in HgTe quantum wells. *Science* **318**, 766–770 (2007).
22. Knez, I. et al. Evidence for helical edge modes in inverted InAs/GaSb quantum wells. *Phys. Rev. Lett.* **107**, 136603 (2011).
23. Hart, S. et al. Induced superconductivity in the quantum spin Hall edge. *Nat. Phys.* **10**, 638–643 (2014).
24. Heedt, S. et al. Signatures of interaction-induced helical gaps in nanowire quantum point contacts. *Nat. Phys.* **13**, 563–567 (2017).
25. Kammhuber, J. et al. Conductance through a helical state in an indium antimonide nanowire. *Nat. Commun.* **8**, 478 (2017).
26. Sanchez-Yamagishi, J. D. et al. Helical edge states and fractional quantum Hall effect in a graphene electron–hole bilayer. *Nat. Nanotechnol.* **12**, 118–122 (2016).
27. Kazakov, A. et al. Electrostatic control of quantum Hall ferromagnetic transition: a step toward reconfigurable network of helical channels. *Phys. Rev. B* **94**, 75309 (2016).
28. Haug, R. J. et al. Quantized multichannel magnetotransport through a barrier in two dimensions. *Phys. Rev. Lett.* **61**, 2797 (1988).
29. Nuebler, J. et al. Quantized $\nu = 5/2$ state in a two-subband quantum Hall system. *Phys. Rev. Lett.* **108**, 46804 (2012).
30. Liu, Y. et al. Evolution of the 7/2 fractional quantum Hall state in two-subband systems. *Phys. Rev. Lett.* **107**, 266802 (2011).
31. Barkeshli, M. & Qi, X. L. Synthetic topological qubits in conventional bilayer quantum Hall systems. *Phys. Rev. X* **4**, 41035 (2014).
32. Bid, A. et al. Observation of neutral modes in the fractional quantum Hall regime. *Nature* **466**, 585–590 (2010).
33. Sabo, R. et al. Edge reconstruction in fractional quantum Hall states. *Nat. Phys.* **13**, 491–496 (2017).
34. Grivnin, A. et al. Nonequilibrated counterpropagating edge modes in the fractional quantum Hall regime. *Phys. Rev. Lett.* **113**, 266803 (2014).

Acknowledgements

We acknowledge Johannes Nübler, Erez Berg, Yuval Oreg, Ady Stern,Yuval Gefen, Jinhong Park, Dmitri Feldman, Kyrylo Snizhko and Onder Gul for fruitful discussions. We thank Diana Mahalu for the e-beam processing and Vitaly Hanin for the help in the ALD process. M.H. acknowledges the partial support of the Israeli Science Foundation (ISF), the Minerva foundation, the US–Israel Bi-National Science Foundation (BSF), the European Research Council under the European Community's Seventh Framework Program (FP7/2007–2013)/ERC Grant agreement 339070 and the German–Israeli Project Cooperation (DIP).

The data that support the plots within this paper and other findings of this study are available from the corresponding author upon reasonable request.

Author contributions

Y.C. and Y.R. contributed equally to this work in heterostructure design, sample design, device fabrication, measurement set-up, data acquisition, data analysis and interpretation, and writing of the paper. D.B. contributed in heterostructure simulation, data analysis and interpretation, and writing of the paper. M.H. contributed in heterostructure design, sample design, data interpretation and writing of the paper. V.U. contributed in heterostructure design and molecular beam epitaxy growth.

Competing interests

The authors declare no competing financial interests.

Additional information

Supplementary information is available for this paper at https://doi.org/10.1038/s41567-017-0035-2.

Reprints and permissions information is available at www.nature.com/reprints.

Correspondence and requests for materials should be addressed to M.H.

Publisher's note: Springer Nature remains neutral with regard to jurisdictional claims in published maps and institutional affiliations.

© 2018 Macmillan Publishers Limited, part of Springer Nature. All rights reserved.

Methods

Sample fabrication. An etch-defined Hall bar with NiGeAu ohmic contacts was fabricated using e-beam lithography. This was followed by an atomic layer deposition of HfO_2, e-beam lithography and e-gun evaporation of 5/20 nm Ti/Au top gates. The top gates, each defining a half-plane of the 2DEG, are separated by a gap of 80 nm. Finally, the HfO_2 is etched in small regions of the contacts, connected to the bonding pads by 5/120 nm Ti/Au leads.

© 2018 Macmillan Publishers Limited, part of Springer Nature. All rights reserved.